

# Honeycomb Structure Inspired Triboelectric Nanogenerator for Highly Effective Vibration Energy Harvesting and Self-Powered Engine Condition Monitoring

Xiu Xiao, Xiangqian Zhang, Siyuan Wang, Han Ouyang, Pengfei Chen, Ligu Song, Haichao Yuan, Yulong Ji, Peihong Wang, Zhou Li,\* Minyi Xu,\* and Zhong Lin Wang\*

Vibration in mechanical equipment can serve as a sustainable energy source to power sensors and devices if it can be effectively collected. In this work, a honeycomb structure inspired triboelectric nanogenerator (HSI-TENG) consisting of two copper electrode layers with sponge bases and one honeycomb frame filled with polytetrafluoroethylene (PTFE) balls is proposed to harvest vibration energy. The application of a compact honeycomb structure increases the maximum power density of HSI-TENG by 43.2% compared to the square grid structure and provides superior advantages in large-scale manufacturing. More importantly, the nonspring-assisted HSI-TENG can generate electricity once the PTFE balls obtain sufficient kinetic energy to separate from the bottom electrode layer regardless of the vibration frequency and direction. This is fundamentally different from the spring-assisted harvesters that can only work around their natural frequencies. The vibration model and working criteria of the HSI-TENG are established. Furthermore, the HSI-TENG is successfully used to serve as a self-powered sensor to monitor engine conditions by analyzing the electrical output of the HSI-TENG installed on a diesel engine. Therefore, the nonspring-assisted HSI-TENG provides a novel strategy for highly effective vibration energy harvesting and self-powered machinery monitoring.

effectively utilized, additional appreciable energy will be generated to supply power for microelectronics, electronic monitoring devices and small sensors. Nanogenerator provides a practical way for harvesting vibration energy and transforming vibration into electricity. Up to now, various vibration-based energy harvesters (VEH) have been developed based on electromagnetic effect,<sup>[1–5]</sup> piezoelectric effect<sup>[6–10]</sup> and electrostatic effect.<sup>[11,12]</sup> But the widespread application of these techniques has met several severe challenges, especially the fabrication of high-quality materials and the stochastic of ambient vibrations. Recently, a brand new energy technology named triboelectric nanogenerator (TENG) has been invented. It works based on the coupling effects of contact electrification and electrostatic induction.<sup>[13–17]</sup> Due to its unique working mechanism, the TENG has proven to be a simple, effective and economical energy harvesting technique.<sup>[18–25]</sup> In addition, the TENG can also use its own electrical output to serve as a self-powered active sensor.<sup>[26–32]</sup>

## 1. Introduction

There are various types of vibration energy in our living environment at anytime and anywhere, such as engines, bridges, vehicles, buildings, etc. Once these discarded energies are

Many research efforts have been devoted to develop various TENG structures for both efficient vibration energy harvesting and self-powered sensing. Most of the vibration energy scavengers are designed as spring-assisted systems, such as the harmonic resonator-based TENG,<sup>[33]</sup> STENG,<sup>[34]</sup> and CF-TENG,<sup>[35]</sup>

Dr. X. Xiao, X. Zhang, S. Wang, Dr. L. Song, H. Yuan, Prof. Y. Ji, Prof. M. Xu  
Marine Engineering College  
Dalian Maritime University  
Dalian 116026, China  
E-mail: xuminyi@dlmu.edu.cn

H. Ouyang, P. Chen, Prof. Z. Li, Prof. Z. L. Wang  
Beijing Institute of Nanoenergy and Nanosystems  
Chinese Academy of Sciences  
Beijing 100085, China  
E-mail: zli@binn.cas.cn; zlwang@gatech.edu

Prof. P. Wang  
School of Physics and Materials Science  
Anhui University  
Hefei, Anhui 230601, China

Prof. Z. L. Wang  
School of Materials Science and Engineering  
Georgia Institute of Technology  
Atlanta, GA 30332-0245, USA

Prof. Z. L. Wang  
College of Nanoscience and Technology  
University of Chinese Academy of Sciences  
Beijing 100049, China

 The ORCID identification number(s) for the author(s) of this article can be found under <https://doi.org/10.1002/aenm.201902460>.

DOI: 10.1002/aenm.201902460

since such systems can provide large amplitude motion and high power output when they are driven at their natural frequencies. However, this kind of TENG has two major limitations. First, the working bandwidths of the spring-assisted TENGs are typically narrow, which restrain their applications in ambient with varying vibration spectra. Second, most of these aforementioned spring-assisted TENGs could only harvest vibration from one direction. Regarding of these two issues, several researchers have tried to improve the working performance of the vibration-based TENG. Bhatia et al.<sup>[36]</sup> proposed a tandem TENG structure for harvesting vibration energy under a wide band of input frequencies. However, the tandem design resulted in a relatively bulky volume and the TENG could only work along one vibration direction. Yang et al.<sup>[37]</sup> demonstrated a 3D-TENG that can scavenge vibration energy in the out-of-plane and in-plane directions. The device had a wide working bandwidth up to 75 Hz in the out-of-plane direction but this value decreased to 14.4 Hz in in-plane directions. Xu et al.<sup>[38]</sup> designed a TENG integrated with a spring (S-TENG) by fabricating a helical structure along the spring wire. Such an S-TENG could harvest both vertical and horizontal vibration energy, but the working bandwidth remained a great challenge.

The main problems of these aforementioned TENGs derived from the resonance characteristic of the spring system, thus the TENGs without spring assistance were proposed by several researchers recently. Xi et al.<sup>[24]</sup> designed a TENG using spherical pellets as the media for performing the contact-separation operation. The device was successfully used to harvest vibration energy excited by ultrasonic wave. But the research parameter was almost exclusively limited to the amount of ultrasonic energy and the vibration characteristics of the system were not considered. He and his co-workers<sup>[25]</sup> proposed a square-grid triboelectric nanogenerator (SG-TENG) for harvesting vibrational energy and sensing impulsive forces. The SG-TENG could harvest vibration energy over a broad bandwidth (10–180 Hz) and operate at different vibration angles, whereas the output peak voltage and current only reached 5.66 V and 0.41  $\mu$ A, respectively. Cheng et al.<sup>[39]</sup> reported an interesting approach to increase the output power of spherical TENGs. By using the liquid/silicone soft balls as the triboelectric layer, the maximum output charge presented up to tenfold enhancement compared to the conventional PTFE balls. It can be seen that the TENGs without spring assistance have provided new way to improve the working performance of TENG. But it is still highly desired to optimize the structure design of nonspring-assisted TENG and systematically characterize the output performance of the TENG.

In the present work, we designed a honeycomb structure inspired triboelectric nanogenerator. The HSI-TENG was composed of two flexible copper electrode layers and one intermediate honeycomb frame fabricated by a 3D printer. The structure was then encapsulated by two parallel acrylic plates. Each of the honeycomb grooves was filled with a Polytetrafluoroethylene ball acting both as the oscillator and triboelectric layer. It is found that the compact honeycomb structure increases the maximum power density by 43.2% compared to the square grid structure. Different from the spring-assisted TENG, the HSI-TENG showed strong frequency adaptability. Under external vibration conditions, the HSI-TENG can

generate electricity once the PTFE balls get sufficient mechanical energy to leave the bottom electrode layer, regardless of the vibration frequency and direction. Based on the theoretical analysis and experimental results, we proposed a bandgap (out of which the HSI-TENG can be triggered) criteria model to demonstrate the work space of HSI-TENG clearly. Furthermore, by applying the newly designed HSI-TENG to the diesel engine of a real ship, we demonstrated that the HSI-TENG can be utilized as an active self-powered sensor to monitor engine condition effectively. The remarkable performances enable the HSI-TENG to have great potentials in vibration energy harvesting and machinery monitoring.

## 2. Results and Discussion

### 2.1. Structure and Working Principle of HSI-TENG

Figure 1 shows the schematic diagram and working principle of the HSI-TENG. The honeycomb frame with PTFE balls inside the grooves is fixed between two parallel copper electrode layers. The frame is then encapsulated by two acrylic plates, forming a typical sandwich structure as shown in Figure 1a,b. Sponge bases are applied between the copper films and acrylic plates to improve the work performance as well as the robustness of the HSI-TENG. The PTFE balls in the honeycomb frame serve both as the oscillator and the electronegative triboelectric layer.

Figure 1c depicts the working mechanism of HSI-TENG. When the PTFE ball is in contact with the bottom copper film, electrons are transferred from the bottom electrode layer to the PTFE ball, resulting in positive and negative triboelectric charges on the surfaces of electrode layer and PTFE ball, respectively (Figure 1ci). As the HSI-TENG is subjected to an external vibration, the PTFE ball starts to move upward and the contacted surface is separated. During this process, the potential of the top electrode is higher than the bottom electrode and electrons begin to transfer from the top to the bottom in the external circuit (Figure 1cii). Once the PTFE ball reaches the top electrode layer, electrons are transferred to the top electrode layer (Figure 1ciii). Finally, when the ball moves downward, electrons start their reverse transfer in the external circuit (Figure 1cvi). Thus, the periodical voltage, current, and transfer charge signals can be generated due to the alternating flow of electrons between the top and bottom electrode layers. To further illustrate the working principle of the HSI-TENG, the potential distribution of the HSI-TENG was calculated from a finite-element simulation using Comsol Multiphysics software. In the simulation, the distance between the top and bottom electrodes was set to 7 mm, the diameter of the PTFE balls was 5 mm, and the electric charge density on the surface of the PTFE ball was 26  $\mu$ C m<sup>-2</sup>. The simulation result is demonstrated in Figure 1d. Apparently, the variation of potential distribution is in consistent with the above analysis. According to the theory behind the contact-mode freestanding TENG, the governing equation for HSI-TENG can be written as<sup>[40]</sup>

$$V = -\frac{Q}{C} + V_{oc} = -\frac{(d_0 + g)}{\epsilon_0 S} Q + \frac{2\sigma x}{\epsilon_0} \quad (1)$$

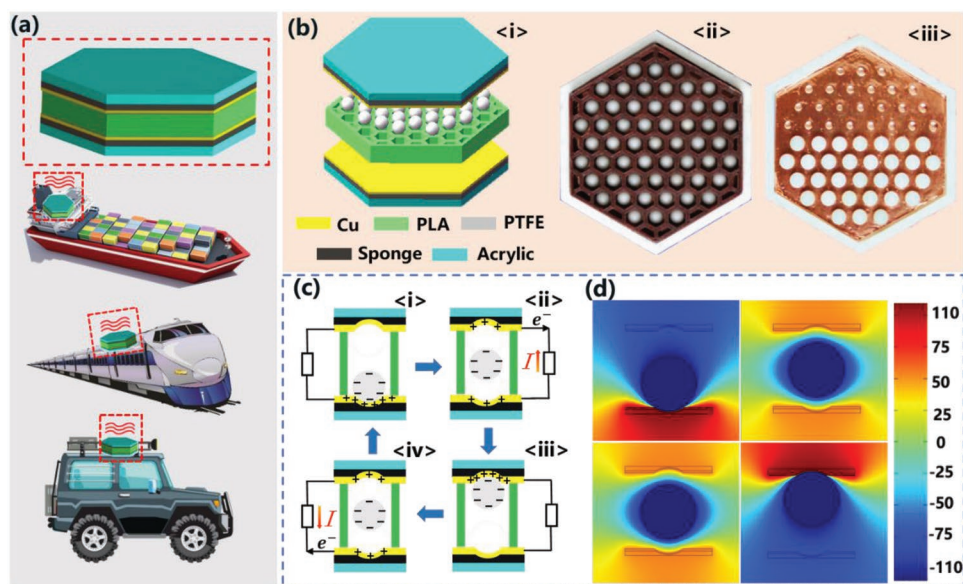


**Figure 1.** Structure and working principle of the HSI-TENG. a) Schematic illustration of the HSI-TENG for vibration energy harvesting. b) Structure of the HSI-TENG. Insets: i) Schematic diagram of the HSI-TENG; ii) image of the honeycomb frame filled with PTFE balls; iii) concaves on the copper electrode layer generated by collision of PTFE balls. c) Working mechanisms of the HSI-TENG. d) The potential distribution across two parallel electrodes at different states calculated by COMSOL Multiphysics software based on finite-element simulation.

where  $V_{OC}$  and  $Q$  are the open-circuit voltage and transfer charge, respectively.  $C$  is the capacitance,  $d_0$  is the effective dielectric thickness,  $g$  is the total air gap thickness between two parallel electrode layers, which is also the thickness of the honeycomb frame in the HSI-TENG,  $\epsilon_0$  is the dielectric constant in vacuum,  $S$  is the area of the copper electrode layer,  $x$  is the separation distance between the electrode layer and the PTFE ball surface, and  $\sigma$  is the charge density.

## 2.2. Performance of HSI-TENG

To evaluate its electrical output performance, the HSI-TENG is mounted on an electrodynamic shaker which can generate sinusoidal vibration with tunable frequency and amplitude, as shown in **Figure 2a**. According to the characteristics of simple harmonic motion, the vibration displacement ( $y$ ) of the HSI-TENG has the expression of  $y = A \sin(\omega t + \varphi)$ , where  $A$  is the vibration amplitude,  $\omega$  is the angular velocity,  $t$  is the transient time and  $\varphi$  is the initial phase angle. The vibration acceleration ( $a$ ) of the device can be written as  $a = -A\omega^2 \sin(\omega t + \varphi)$ . Thus, the relationship between the maximum vibration acceleration ( $a_m$ ), the vibration frequency ( $f$ ) and the vibration amplitude ( $A$ ) is  $a_m = A(2\pi f)^2$ , which is depicted in **Figure 2b**.

**Figure 2c** shows the output open-circuit voltage ( $V_{OC}$ ) of HSI-TENG as the vibration frequency increases from 10 to 60 Hz. The displacement stroke  $\Delta x$  of the PTFE ball is 2.0 mm and the vibration amplitude  $A$  is fixed at 0.5 mm. The vibration angle, which is the angle between the vibration direction and the water level, is  $90^\circ$ . The corresponding output short-circuit current ( $I$ ) and transfer charge ( $Q$ ) of HSI-TENG are described in **Figure S1b,c** (Supporting Information). Three distinctive working features can be seen from these figures. First, the HSI-TENG cannot produce electrical output when the vibration

frequency is less than about 20 Hz. As above mentioned, the HSI-TENG works based on the freestanding contact-separation mode between the triboelectric layers. When the device vibrates in vertical direction with vibration acceleration lower than about  $9.8 \text{ m s}^{-2}$  (with the corresponding frequency of 22.28 Hz), the PTFE balls cannot get enough mechanical energy to overcome gravity effect and to separate with the bottom electrode layer. As a result, there is no electron transfer in the external circuit. Thus, there exists a bandgap in which the HSI-TENG cannot be triggered. Second, the output voltage increases rapidly when the vibration frequency is increased from 25 to 35 Hz. At this stage, the PTFE balls start to collide up and down between the two electrode layers as driven by the vibration. The change in the electrical output is caused by the increase of contact force and the effective contact area between the triboelectric layers.<sup>[41]</sup> Third, the output voltage and transfer charge basically keep constant (i.e.,  $V_{OC} = 78 \text{ V}$  and  $Q = 27 \text{ nC}$ ) when the vibration frequency is greater than 35 Hz. Under such condition, the effective contact area between the electrode layers and the PTFE balls is maximized and the electrical output of the HSI-TENG does not change with the vibration frequency anymore. It reveals that the HSI-TENG has excellent frequency adaptability and it is capable of harvesting vibration energy as long as the vibration acceleration exceeds a certain value for the spring-assisted TENGs that only work around their resonance frequencies.<sup>[33–35]</sup>

To further investigate the performance of HSI-TENG, the electrical output is also measured while the electrodynamic shaker vibrates with a constant maximum acceleration ( $a_m$ ). As shown in **Figure 2d**, the output voltage decreases continuously as the vibration frequency increases from 10 to 35 Hz. Similar tendency can be found in the transfer charge profile while the short-circuit current experiences a process of increasing and

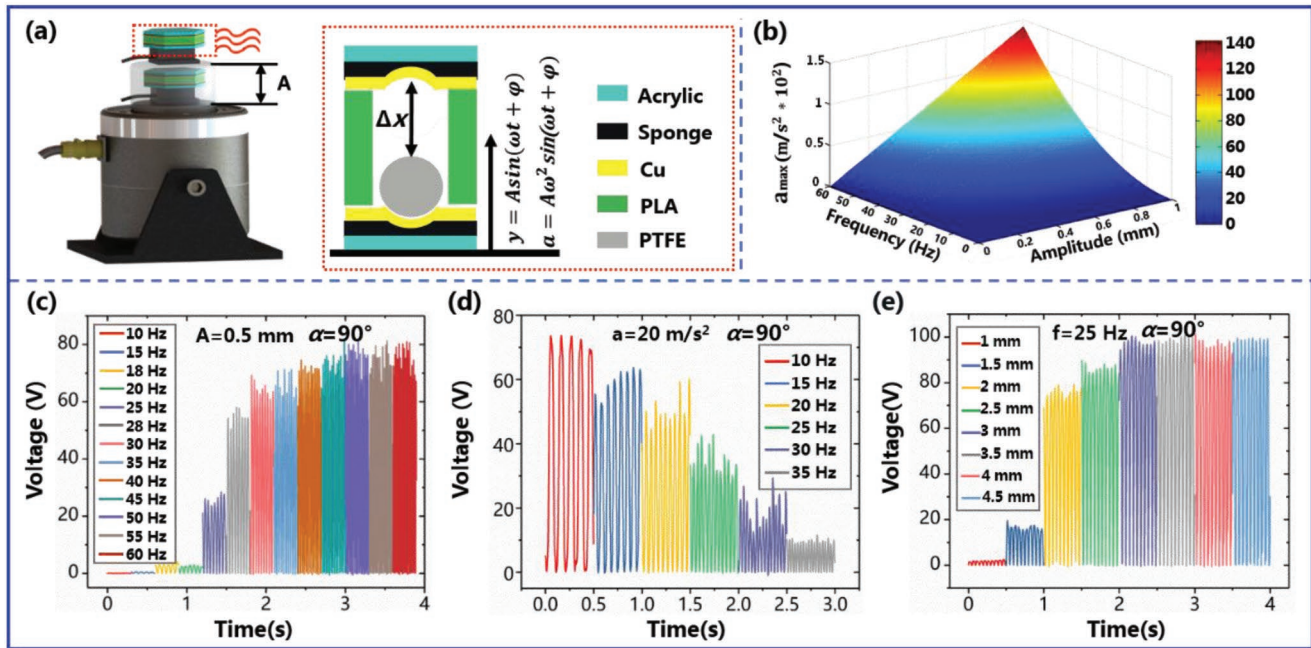


**Figure 2.** Output performance of HSI-TENG vibrating in vertical direction. a) Schematic of the HSI-TENG on an electrodynamic shaker. b) Relationship between the maximum vibration acceleration, vibration amplitude and vibration frequency. Output voltage of the HSI-TENG working c) at different frequencies with a fixed vibration amplitude of 0.5 mm, d) at different frequencies with a fixed vibration acceleration of 20 m s<sup>-2</sup>, and e) at different amplitudes with a fixed vibration frequency of 25 Hz.

then decreasing (Figure S1d,e, Supporting Information). It owes to the fact that the vibration amplitude of HSI-TENG is reduced in square relationship with the increase of vibration frequency. For  $a_m = 20 \text{ m s}^{-2}$ , the vibration amplitude is reduced to 0.41 mm when the vibration frequency reaches 35 Hz. Under the vibration condition with a minor amplitude, the mechanical energy accumulated by the PTFE balls is quite limited. Considering that the output performance of HSI-TENG is positively correlated with the collision force between the copper electrode layer and the PTFE ball, the electrical output decreases along with the vibration amplitude. Additionally, Figure 2e depicts the variation of output voltage with the vibration amplitude when the vibration frequency is kept at 25 Hz. It can be seen that as the vibration amplitude increases from 1.0 to 4.5 mm, the output voltage has gone through two stages that are characterized by rapid increase and stable output with high value ( $V_{OC} = 98 \text{ V}$ ). The profiles of short-circuit current and transfer charge are exhibited in Figure S1g,h (Supporting Information). Since the vibration acceleration increases linearly with the vibration amplitude when the frequency is kept constant, the PTFE balls in the honeycomb grooves can get more kinetic energy when the vibration amplitude is increased from 1.0 to 2.0 mm. Thus, large voltage variations are observed under such circumstances. But with the further increase of vibration amplitude, the effective contact area between the copper electrode layers and the PTFE balls reaches its maximum. Consequently, the electrical output tends to saturate.

From the above measurements, it can be concluded that vibration acceleration and vibration amplitude are two critical parameters that determine the work performance of HSI-TENG and there exists a bandgap in which the HSI-TENG cannot

be triggered. This phenomenon is one of the most important working characteristics of HSI-TENG. Therefore, we take a further step to make a theoretical analysis on the width of the bandgap. Taking into account that the HSI-TENG has a honeycomb structure and the movements of PTFE balls in each of the grooves are completely identical, we only demonstrate the working boundary of one PTFE ball for clarification. From the perspective of energy conversion, the total mechanical energy ( $E_t$ ) that is transferred to the PTFE ball from the electrodynamic shaker consists of three parts, which are kinetic energy ( $E_k$ ), gravitational potential energy ( $E_p$ ) and the energy loss caused by collision and friction ( $E_l$ ), respectively. Thus, the energy conservation equation can be written as

$$E_t = E_k + E_p + E_l \quad (2)$$

According to Newton's second law of motion,  $E_t$  has the expression of  $E_t = \int_{-A}^A m_0 \cdot a(\gamma) d\gamma = m_0 \cdot a_m \cdot A$ , where  $m_0$  is the mass of one PTFE ball, and  $\gamma$  is the vibration displacement. It is reasonable to assume that the PTFE ball starts to leave the bottom electrode layer when the HSI-TENG vibrates to the maximum vibration displacement. Thus, the gravitational potential energy obtained by the PTFE ball is linearly related to the vibration amplitude and can be given as  $E_p = m_0 \cdot g \cdot 2A$ . The HSI-TENG starts to work only if the PTFE ball gets sufficient kinetic energy to leave the bottom electrode layer and to collide with the top electrode layer. Therefore, the kinetic energy  $E_k$  has the equivalent expression of  $E_k = \frac{1}{2} m_0 \cdot v^2 = m_0 \cdot g \cdot (\Delta x - c \cdot A)$ , where  $v$  is the velocity at which the PTFE ball leaves the bottom layer and  $\Delta x$  is the displacement stroke of the PTFE ball as shown

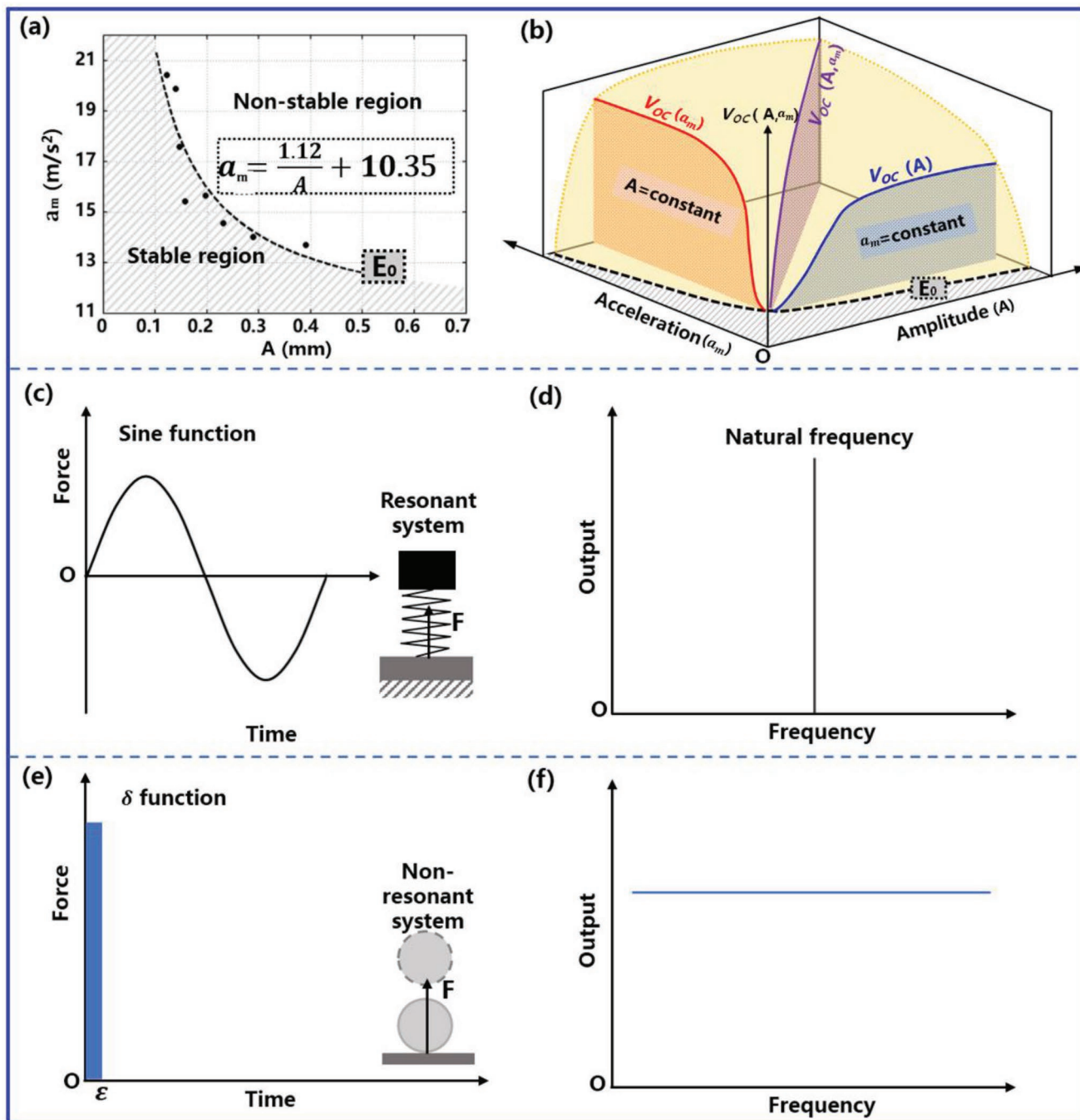


**Figure 3.** Workspace and working characteristics of HSI-TENG. a) The bandgap criteria of HSI-TENG. b) Schematic diagram of the workspace and output performance of HSI-TENG. c) Force analysis of the spring-assisted TENG system. d) The resonant frequency of the spring-assisted TENG system. e) Force analysis of the PTFE ball in HSI-TENG. f) Frequency adaptability of the HSI-TENG system.

in Figure 2a. Here, a coefficient  $c$  is adopted to consider the relative motion between PTFE ball and the honeycomb frame. Under such critical state, the energy loss  $E_1$  is limited and can be neglected (i.e.,  $E_1 = 0$ ). Based on the above assumptions and analysis, the energy conversion relationship for unit mass is

$$a_m = \frac{g\Delta x}{A} + (2-c)g \quad (3)$$

In other words, Equation (3) represents the critical vibration boundary of the HSI-TENG beyond which the device starts to harvest vibrational energy effectively. To further clarify the bandgap model, the output performance of HSI-TENG at different vibration frequencies is measured with the open-circuit voltage of 1 V taken as the criteria. The scatter points in Figure 3a represent the working boundary of HSI-TENG acquired from experimental measurements. As expected, the

maximum vibration acceleration is a function of vibration amplitude and the two parameters change inversely. By fitting experimental data, the boundary equation of the HSI-TENG is obtained as  $a_m = \frac{1.12}{A} + 10.35$ . According to the relationship between the mechanical energy and the maximum vibration acceleration, the critical mechanical energy for PTFE balls to separate from the bottom electrode layers can be expressed as

$$E_0 = m_0 \cdot a_m \cdot A = m_0 (1.12 + 10.35A) \quad (4)$$

It is worth noting that as an important working characteristic of the present HSI-TENG, the bandgap can also be used to increase the signal-to-noise ratio of the device, which will be discussed in our future study.

In addition to the bandgap, frequency adaptability is another distinctive working feature of HSI-TENG. Figure 3b displays the comprehensive working performance of HSI-TENG. The three colored solid lines in this figure represent the output tendencies of vibration amplitude response (red line), the acceleration response (blue line) and the combined response (purple line), respectively. The detailed output voltage variation obtained from experimental measurements can be found in Figure S2 (Supporting Information). As illustrated in Figure 3b, once the vibration parameters outrange the bandgap, the output voltage reaches a plateau after a rapid increase and the device exhibits an excellent and stable output performance that is independent of vibration frequency. This outstanding advantage provides great potential application of HSI-TENG for harvesting vibration energy with varying vibration spectra.

The independence of electrical output with respect to vibration frequency can be further explained by Fourier analysis. The ideal vibration characteristic of the typical spring-assisted resonant TENG system with single degree of freedom is also exhibited for comparison. When the spring damping system is subjected to a continuous sinusoidal external excitation force, the TENG will vibrate in small amplitude synchronously. Resonance occurs only when the excitation frequency is equal to the natural frequency of the system, and the vibration amplitude reaches a maximum under such condition. Figure 3c,d shows the time and frequency domains of the spring resonant system. Thus, the working frequency of the spring-assisted TENG is determined by the natural frequency of the resonance system and its working bandwidth is very narrow. Different from the spring-assisted TENG, the present honeycomb structure inspired TENG works due to the relative movement between the PTFE ball and the intermediate structure. The PTFE ball will leave the bottom electrode layer when its mechanical energy is large enough to overcome gravity effect. Under this condition, the ball collides up and down between the electrode plates and it's imposed with periodic discrete force that has the same frequency with the TENG. The instantaneous force in one vibrating cycle has the following expression:

$$F(t) = \begin{cases} P & \text{when } 0 < t < \varepsilon \\ 0 & \text{when } t \geq \varepsilon \end{cases} \quad (5)$$

where  $P$  and  $\varepsilon$  are the magnitude and acting time of the force, respectively. As shown in Figure 3e, the force acts in an

extremely short time (i.e.,  $\varepsilon \rightarrow 0$ ) and thus it has very similar characteristic to the Dirac delta ( $\delta$ ) function. According to Fourier transformation, the frequency domain covers all the vibration frequencies, as displayed in Figure 3f. Therefore, the HSI-TENG can be seen as a nonresonant system and its work-space is independent of vibration frequency. Apparently, this result is consistent with the experimental outcome.

In fact, the application of honeycomb structure not only allows the TENG to harvest vibration energy without being limited by resonance characteristics, but also can improve the electrical output in the following ways. On one hand, the compactness nature of the honeycomb structure increases the effective contact area between PTFE balls and electrode layers. Figure 4a compares the number of grooves in the square-grid frame and the honeycomb frame. It can be seen that for the intermediate frame with a total surface area of  $2.5 \times 10^{-3} \text{ m}^2$  and the PTFE balls with diameter of 5.0 mm, the honeycomb frame has 55 grooves, 6 more than that of the square-grid frame. As a result, the effective contact area is increased by 12.2%. On the other hand, the electrical output of HSI-TENG is positively correlated with the effective contact area. Considering that the effective contact area is determined by the number of PTFE balls, the impact of contact area on output power as well as the scalability of HSI-TENG are investigated by filling the honeycomb grooves with different numbers of PTFE ball ( $n$ ). The results are demonstrated in Figure 4b and Figure S3 (Supporting Information). As shown in Figure S3 (Supporting Information), the electrical output of HSI-TENG, including the open-circuit voltage, short-circuit current and transfer charge, increases significantly with the increase of PTFE balls. The increase in output voltage is mainly caused by the increase of transfer charge. According to the basic theory of electrostatics, the open-circuit voltage of the HSI-TENG can be formulated as  $V_{OC} = Q_{SC}/C$ . With the increase of PTFE balls, the effective contact area between the triboelectric layers is enlarged, which produces more triboelectric charges. As a result, the transfer charge in the external circuit is increased. Based on the relationship between the output voltage and transfer charge described in the above equation, the increase in  $Q_{SC}$  will lead to the increase of  $V_{OC}$ . More specifically, as the number of PTFE ball increases from 1 to 55, the peak voltage, peak current and peak transfer charge increase linearly to 98 V, 3.4  $\mu\text{A}$  and 28.5 nC, respectively (Figure 4b). Compared with the TENG based on square grid structure with the same volume, the open-circuit voltage, short-circuit current and transfer charge of the HSI-TENG are increased by 16.5%, 17.2%, and 14.8%, respectively. Therefore, a higher electrical output is expected as the cross-sectional area of the honeycomb frame as well as the number of PTFE ball increase.

Owing to the unique structure design of HSI-TENG, the device is capable of harvesting vibration energy along various directions. Figure 5a–c shows the frequency response of the peak open-circuit voltage, peak short-circuit current and peak transfer charge of the HSI-TENG at vibration angles of  $0^\circ$ ,  $45^\circ$ , and  $90^\circ$ , respectively. The vibration frequency ranges from 10 to 60 Hz with vibration amplitude fixed at 0.5 mm. Clearly, the HSI-TENG with vibration direction of horizontal will produce more electrical output at lower vibration frequencies and the output difference among various vibration angles disappears as

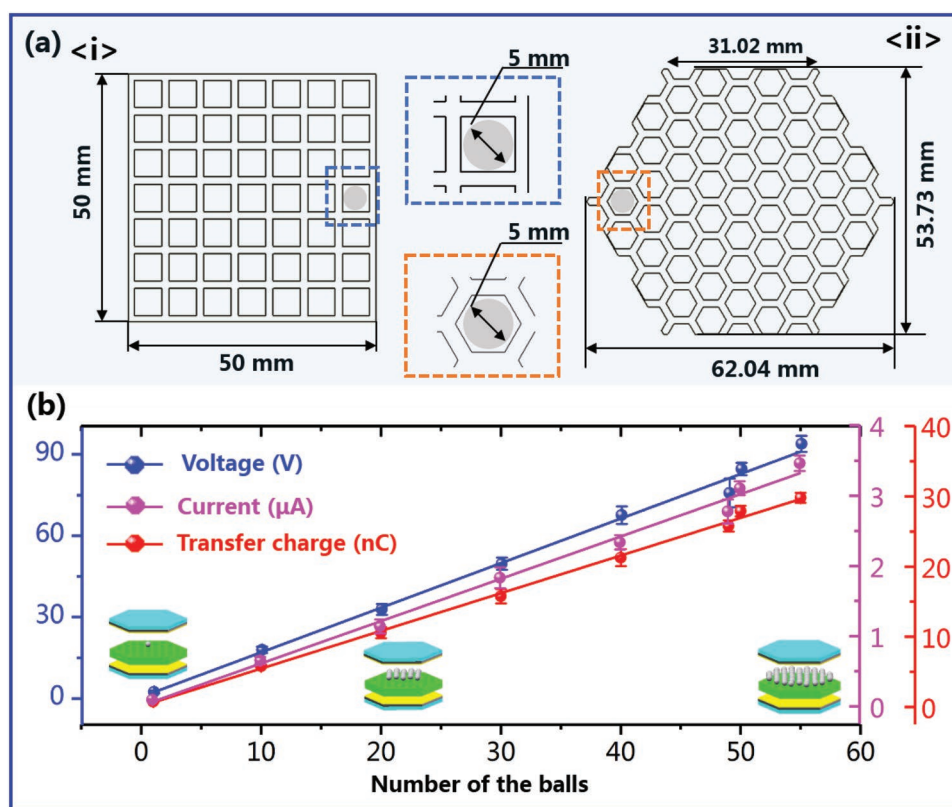


**Figure 4.** Honeycomb structure enhanced electrical output of HSI-TENG. a) Comparison of effective contact area between square-grid structure and honeycomb structure. b) The effect of PTFE ball number on the output of HSI-TENG.

the vibration frequency reaches 35 Hz or higher. It is because, compared with the HSI-TENG working at nonhorizontal directions with low frequencies, the gravity effect in the horizontal HSI-TENG can be ignored and the PTFE balls can get more kinetic energy from the vibration of electrodynamic shaker. As a result, the collision force between the PTFE ball and the electrode layers is greater and more electrical output is generated at  $\alpha = 0^\circ$ . When the vibration frequency exceeds 35 Hz, both of the collision force impact and the effective contact area are maximized, thereby producing substantially the same electrical output ( $V_{OC} = 78$  V) in all vibration directions. In addition to vibration conditions, structural parameters also play a great role in determining the electrical output of HSI-TENG. As mentioned above, HSI-TENG operates in a hybridizational mode of vertical contact–separation and freestanding. Thus, the displacement stroke can be a key parameter that affects the performance of the device. Figure 5d–f compares the peak  $V_{OC}$ ,  $I_{SC}$ , and  $Q$  while the displacement stroke  $\Delta x$  setting to 0.5, 1.0, 2.0, and 4.0 mm, respectively. As can be seen from this figure, the power output achieves its maximum when  $\Delta x = 1.0$  mm and it decreases when the displacement stroke is below or above such value. This result has provided us a guideline for structure optimization design of HSI-TENG in the future.

In conclusion, the as-fabricated HSI-TENG is characterized by its good frequency adaptability and high power density. To better elaborate its distinguished performance in vibration energy harvesting, the working characteristics of the HSI-TENG are compared with the earlier reported vibration-based

energy harvesters. The results are listed in Table S1 in the Supporting Information. It can be seen from the above table that the working range of the as-fabricated nonspring-assisted HSI-TENG is not confined by the natural frequency of spring system and the power density is higher than many of the earlier reported vibration-based TENGs. To further improve the output performance of the HSI-TENG, surface treatment is recommended to introduce nanowire structures on the surface of PTFE balls. The uniformly distributed nanowire features can not only increase the surface roughness and the effective surface area of the TENG for effective triboelectrification, but also enhance the triboelectric charge density of the PTFE balls. In addition, some related works<sup>[39]</sup> have proposed that soft balls with tunable softness can significantly enhance the output charge of the TENG compared to that of the conventional PTFE based one. Although the deformation process of the soft balls will consume vibration energy during TENG operation, this provides a promising way to improve the electrical output of the present HSI-TENG.

### 2.3. Demonstration

Based on the performance of the HSI-TENG presented above, we find that the device is an ideal candidate for vibration energy harvesting. Figure 6 demonstrates the output performance of the HSI-TENG as a direct power source. The TENG is excited by an electrodynamic shaker working at a vibration amplitude

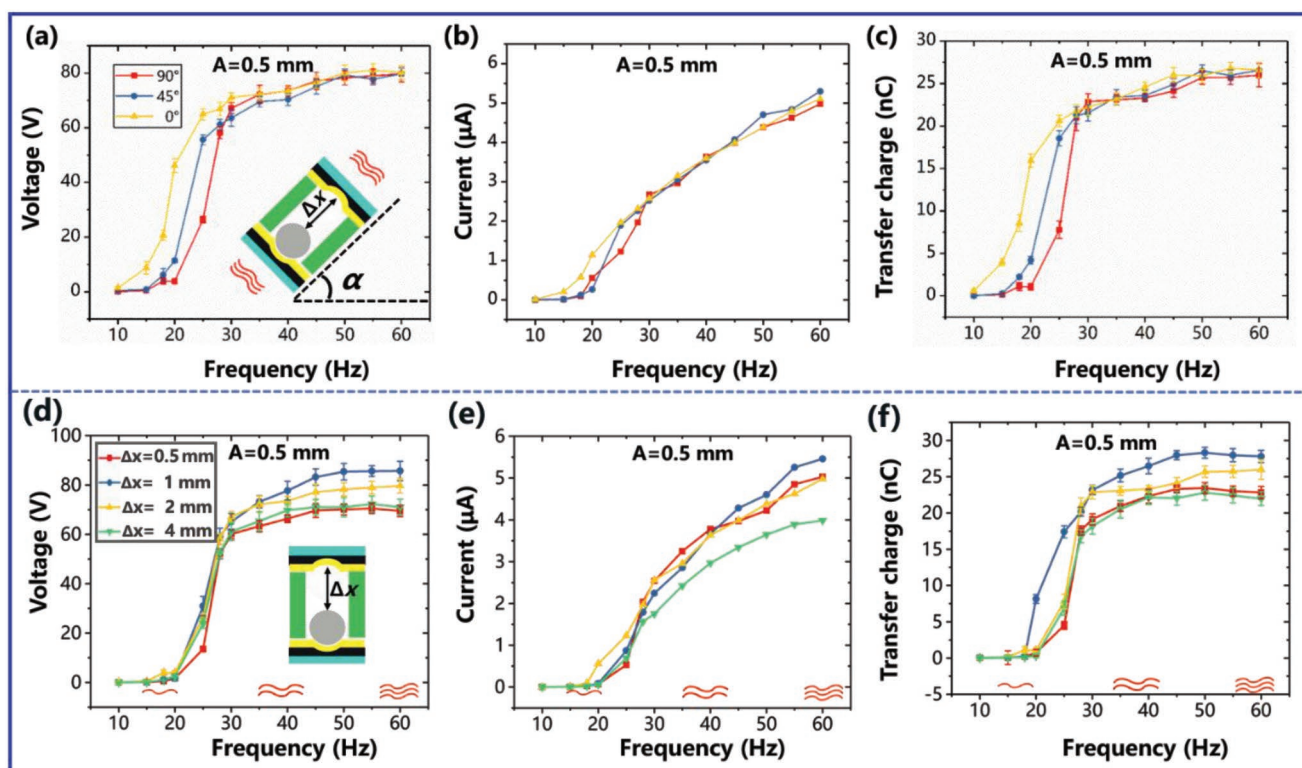


**Figure 5.** Output performance of HSI-TENG working under different vibration directions and displacement strokes. a) The peak voltage ( $V_{OC}$ ), b) peak current ( $I_{SC}$ ), and c) peak transfer charge ( $Q$ ) of HSI-TENG tilted at different vibration angles ( $\alpha = 0^\circ, 45^\circ, 90^\circ$ ) with vibration frequency ranging from 10 to 60 Hz. d) The peak voltage ( $V_{OC}$ ), e) peak current ( $I_{SC}$ ), and f) peak transfer charge ( $Q$ ) of HSI-TENG having different displacement strokes ( $\Delta x = 0.5, 1, 2, 4$  mm) as vibration frequency increases from 10 to 60 Hz.

of 2.0 mm. The honeycomb frame is filled with 55 PTFE balls and the displacement stroke of the PTFE balls is 1.0 mm. Resistors are utilized as external loads to evaluate the output power of HSI-TENG. As plotted in Figure 6a, the current amplitude drops with the increase of load resistance and the output power density is maximized at the load resistance of 200 M $\Omega$  with the corresponding peak value of 50 W m<sup>-3</sup>. Compared to that of the TENG based on square grid structure with the same volume (Figure S4, Supporting Information), the maximum power density is increased by 43.2%. Furthermore, it can be seen from Figure 6b that the capacitors with different capacitances are successfully charged by HSI-TENG. Robustness is another critical criteria for energy harvesters. Thus, the durability test of HSI-TENG is also carried out in this work. The output voltage is consistent over seven days (Figure 6c), implying the device is durable. Furthermore, more than 200 LEDs connected in series can be lit up simultaneously as can be seen in Figure 6d and Video S1 (Supporting Information), demonstrating the capability of HSI-TENG as a sustainable power source. Sensor powering is one of the most important applications of TENG. Figure 6e shows the working circuit of HSI-TENG for vibration energy harvesting to power a sensor. As can be seen from Figure 6f, the temperature sensor is successfully lit up after 80 s charging of the 100  $\mu$ F capacitor. The video for lighting temperature sensor is also shown in Video S1.

In addition to vibration energy harvesting, the HSI-TENG can also serve as a self-powered active sensor for real-time

engine condition monitoring. In this work, the HSI-TENG is fixed to the diesel engine of a real ship named YuKun in China. Figure 6g shows a photo of HSI-TENG being attached to the diesel engine. The output current of the HSI-TENG during the start, stop and normal operation processes of the diesel engine are displayed in Figure 6h and Video S2 (Supporting Information). The results show that the short-circuit current can get to 2  $\mu$ A during normal operation of the diesel engine. Thus, it is conceivable that the amount of power generation will be considerable if multiple HSI-TENGs are networked, which is capable of powering a large number of sensors. More importantly, the working condition of the diesel engine can be obtained by performing fast Fourier transform (FFT) on the real-time current signals of HSI-TENG. It is known that the vibration of the diesel engine is mainly caused by the combustion state in the cylinder. During the normal operation of diesel engine, the piston compresses the combustion gases during the compression stroke and causes a fire, which creates a sudden increase in pressure in the combustion chamber. The Wärt-silä Auxpac 520W4L20 diesel generator that is used in YuKun ship is equipped with four cylinders and rates at 1000 rpm. Each cylinder works 500 (1000/2) times per minute. Therefore, the diesel engine works 2000 times per minute and the theoretical vibration frequency is 33.33 (2000/60) Hz. Figure 6i demonstrates the result of FFT analysis. The magnitude reaches its maximum at about  $f = 33$  Hz, indicating that the dominate vibration frequency of the diesel engine acquired by

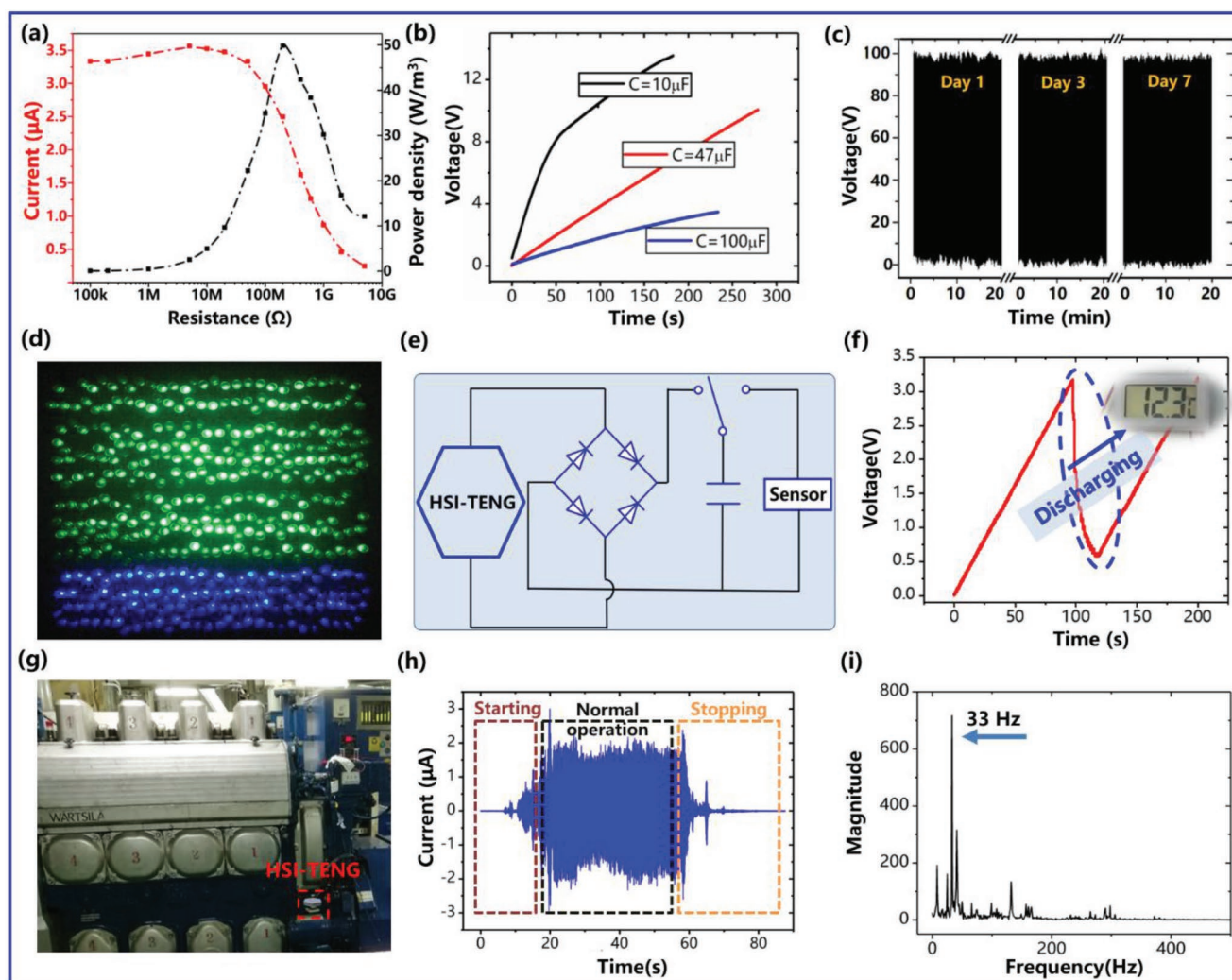


**Figure 6.** Demonstration of the HSI-TENG for vibration energy harvesting and engine condition monitoring. a) Dependence of the voltage and output power on the external load resistance for the HSI-TENG working at vibration frequency of 25 Hz and vibration amplitude of 2.0 mm. b) Voltages of different capacitors ( $C = 10, 47$  and  $100 \mu\text{F}$ ) charged by HSI-TENG. c) The result of robustness test. d) Photograph of more than 200 light-emitting diodes connected in series that are lit up simultaneously by HSI-TENG. e) The working circuit of HSI-TENG for vibration energy harvesting to power sensor. f) Powering a temperature sensor with HSI-TENG. g) Photograph of HSI-TENG as a self-powered monitor for the diesel engine on the ship YuKun. h) The output short-circuit current of HSI-TENG during the start–stop process of the diesel engine. i) The working frequency of the diesel engine acquired by the HSI-TENG as an active sensor.

the HSI-TENG is 33 Hz. It is inspiring to note that this value agrees well with the diesel engine's working frequency. In other words, the HSI-TENG has successfully proved its capability in vibration sensing. Therefore, besides from vibration energy harvesting, the HSI-TENG can also serve as a self-powered vibration sensor for machinery monitoring.

### 3. Conclusion

In this work, we presented a honeycomb structure inspired triboelectric nanogenerator as a vibration energy harvester and a self-powered engine condition monitor. The HSI-TENG is composed of two copper electrode layers with sponge bases and one honeycomb frame as the intermediate port. The PTFE ball filled in each of the honeycomb grooves acts as both the oscillator

and the triboelectric layer. In order to investigate the output performance of HSI-TENG, the device is excited by an electrodynamic shaker with tunable vibration frequency and amplitude. Three distinctive working characteristics were observed. First, HSI-TENG has good frequency adaptability and high power density. Different from the spring-assisted TENGs that only work around their natural frequencies, the HSI-TENG can produce electrical output once the PTFE balls get sufficient kinetic energy. Comparing to the TENG based on square grid structure with the same volume, the maximum power density of HSI-TENG is increased by 43.2%. Second, the criteria of bandgap in which the HSI-TENG cannot be triggered have been proposed by theoretical and experimental methods, which clearly clarifies the workspace of HSI-TENG and provides a promising way to increase the signal-to-noise ratio of the device. Third, the HSI-TENG can effectively scavenge vibration energy from different

vibration directions without significant difference. In conclusion, the newly designed HSI-TENG has exhibited an excellent and stable output performance, making it a great candidate for vibration energy harvesting. Additionally, the HSI-TENG can also serve as a robust self-powered engine condition monitor. The FFT analysis indicates that the operation frequency of the diesel engine on the ship YuKun were accurately acquired by HSI-TENG. This successful application indicates the great potential of HSI-TENG for machinery monitoring.

## 4. Experimental Section

**Fabrication of HSI-TENG:** The schematic diagram of the newly designed HSI-TENG is shown in Figure 1a,b. The device consists of a honeycomb structure frame, PTFE balls and two copper electrode layers fixed on acrylic plates through sponge bases. The copper electrode layer has a thickness of 0.2 mm. The intermediate honeycomb frame that is made of polylactic acid material is printed by a 3D printer. A total of 55 grooves is formed on the honeycomb structure and the cross section of each groove is a regular hexagon. For each groove, a PTFE ball with diameter of 5.0 mm is filled inside to act as both the oscillator and the electronegative triboelectric layer. The PTFE is chosen considering its three superior material properties. First, the PTFE material has very good triboelectrification effect and a high electron negativity. According to the quantified triboelectric series reported by Zou et al.,<sup>[42]</sup> the normalized triboelectric charge density of PTFE can reach  $-113 \mu\text{Cm}^{-2}$ . Second, the density of the PTFE is very small and the PTFE balls are thus light in weight. Considering that the critical vibration acceleration is proportional to the mass of the PTFE balls, this material property can increase the vibration sensitivity of TENG. Third, the PTFE balls are very firm and not easy to break. During the operation of the HSI-TENG, the PTFE balls collide up and down between the two electrode plates as driven by the vibration. Such a physical property can enhance the robustness of the TENG. The sponge bases on the electrode layers can improve the work performance of HSI-TENG from two aspects. On the one hand, the robustness and durability of the device is significantly enhanced since the sponge bases can absorb the energy of PTFE balls and thus protect the electrode layers from rupturing. On the other hand, owing to the enlargement of effective contact surface, the transfer charge is increased by about 30% compared with the HSI-TENG without sponge bases (Figure S5, Supporting Information).

**Electrical Output Measurements:** When measuring the electrical output of HSI-TENG, the device is mounted on an electrodynamic shaker (JZK-10), which is driven by an amplified sinusoidal wave from a function generator (YE1311) and an amplifier (YE5852). The electrode layers remain perpendicular to vibration direction when the shaker is tilted at different angles. The output signals including the open-circuit voltage, short-circuit current and transfer charges are measured by Keithley 6514 electrometer.

## Supporting Information

Supporting Information is available from the Wiley Online Library or from the author.

## Acknowledgements

X.X. and X.Z. contributed equally to this work. Supports from the National Natural Science Foundation of China (Grant Nos. 51879022, 51979045, 61875015, and 51906029), the Fundamental Research Funds for the Central Universities, China (Grants Nos. 3132019197, 3132019196, and 3132019037), the National Key Research and

Development Program of China (Grant No. 2016YFA0202704), the “Thousands Talents” program for pioneer researcher and his innovation team in China, Projects for Dalian Youth Star of Science and Technology (Grant No. 2018RQ12) and the Young Elite Scientists Sponsorship Program by CAST (Grant No. 2016QNRC001) are appreciated.

## Conflict of Interest

The authors declare no conflict of interest.

## Keywords

bioinspired, self-powered sensor, triboelectric nanogenerators, vibration energy harvesting

Received: July 28, 2019

Revised: August 22, 2019

Published online:

- [1] S. D. Kwon, J. Park, K. Law, *Smart Mater. Struct.* **2013**, *22*, 12.
- [2] X. Y. Wang, S. Palagummi, L. Liu, F. G. Yuan, *Smart Mater. Struct.* **2013**, *22*, 10.
- [3] X. L. Bai, Y. M. Wen, J. Yang, P. Li, J. Qiu, Y. Zhu, *J. Appl. Phys.* **2012**, *111*, 3.
- [4] M. A. Halim, H. Cho, M. Salauddin, J. Y. Park, *Sens. Actuators, A* **2016**, *249*, 23.
- [5] P. Wang, K. Tanaka, S. Sugiyama, X. Dai, X. Zhao, J. Liu, *Microsyst. Technol.* **2009**, *15*, 941.
- [6] Z. L. Wang, J. H. Song, *Science* **2006**, *312*, 242.
- [7] X. D. Wang, *Nano Energy* **2012**, *1*, 13.
- [8] X. N. Wen, W. Z. Wu, Y. Ding, Z. L. Wang, *Adv. Mater.* **2013**, *25*, 3371.
- [9] R. A. Whiter, V. Narayan, S. Kar-Narayan, *Adv. Energy Mater.* **2014**, *4*, 1400519.
- [10] S. Crossley, S. Kar-Narayan, *Nanotechnology* **2015**, *26*, 344001.
- [11] H. Okamoto, Y. Hamate, L. Xu, H. Kuwano, *Smart Mater. Struct.* **2012**, *21*, 065001.
- [12] Y. Chiu, Y.-C. Lee, *J. Micromech. Microeng.* **2013**, *23*, 015012.
- [13] F. R. Fan, Z. Q. Tian, Z. L. Wang, *Nano Energy* **2012**, *1*, 328.
- [14] R. Hinchet, A. Ghaffarinejad, Y. X. Lu, J. Y. Hasani, S. W. Kim, P. Basset, *Nano Energy* **2018**, *47*, 401.
- [15] W. Liu, Z. Wang, G. Wang, G. Liu, J. Chen, X. Pu, Y. Xi, X. Wang, H. Guo, C. Hu, Z. L. Wang, *Nat. Commun.* **2019**, *10*, 1426.
- [16] J. Nie, Z. Wang, Z. Ren, S. Li, X. Chen, Z. Lin Wang, *Nat. Commun.* **2019**, *10*, 2264.
- [17] J. Nie, X. Chen, Z. L. Wang, *Adv. Funct. Mater.* **2018**, 1806351.
- [18] X. M. He, H. Y. Guo, X. L. Yue, J. Gao, Y. Xia, C. G. Hu, *Nanoscale* **2015**, *7*, 1896.
- [19] Y. L. Zi, J. Wang, S. H. Wang, S. M. Li, Z. Wen, H. Y. Guo, Z. L. Wang, *Nat. Commun.* **2016**, *7*, 8.
- [20] X. Zhang, M. Yu, Z. Ma, H. Ouyang, Y. Zou, S. L. Zhang, H. Niu, X. Pan, M. Xu, Z. Li, Z. L. Wang, *Adv. Funct. Mater.* **2019**, 1900327.
- [21] G. Cheng, Z. H. Lin, Z. L. Du, Z. L. Wang, *ACS Nano* **2014**, *8*, 1932.
- [22] G. H. Lim, S. S. Kwak, N. Kwon, T. Kim, H. Kim, S. M. Kim, S. W. Kim, B. Lim, *Nano Energy* **2017**, *42*, 300.
- [23] M. Xu, T. Zhao, C. Wang, S. L. Zhang, Z. Li, X. Pan, Z. L. Wang, *ACS Nano* **2019**, *13*, 8.
- [24] Y. Xi, J. Wang, Y. L. Zi, X. G. Li, C. B. Han, X. Cao, C. G. Hu, Z. L. Wang, *Nano Energy* **2017**, *38*, 101.
- [25] L. Xu, T. Jiang, P. Lin, J. J. Shao, C. He, W. Zhong, X. Y. Chen, Z. L. Wang, *ACS Nano* **2018**, *12*, 1849.

- [26] Y. Yang, L. Lin, Y. Zhang, Q. S. Jing, T. C. Hou, Z. L. Wang, *ACS Nano* **2012**, *6*, 10378.
- [27] Q. Jing, G. Zhu, W. Wu, P. Bai, Y. Xie, R. P. S. Han, Z. L. Wang, *Nano Energy* **2014**, *10*, 305.
- [28] H. Y. Mi, X. Jing, Q. F. Zheng, L. M. Fang, H. X. Huang, L. S. Turng, S. Q. Gong, *Nano Energy* **2018**, *48*, 327.
- [29] M. Xu, S. Wang, S. L. Zhang, W. Ding, P. T. Kien, C. Wang, Z. Li, X. Pan, Z. L. Wang, *Nano Energy* **2019**, *57*, 574.
- [30] R. Hinchet, W. Seung, S.-W. Kim, *ChemSusChem* **2015**, *8*, 2327.
- [31] H. Guo, X. Pu, J. Chen, Y. Meng, M.-H. Yeh, G. Liu, Q. Tang, B. Chen, D. Liu, S. Qi, C. Wu, C. Hu, J. Wang, Z. L. Wang, *Sci. Rob.* **2018**, *3*, eaat2516.
- [32] Z. Ren, J. Nie, L. Xu, T. Jiang, B. Chen, X. Chen, Z. L. Wang, *Adv. Funct. Mater.* **2018**, *28*, 1805277.
- [33] J. Chen, G. Zhu, W. Q. Yang, Q. S. Jing, P. Bai, Y. Yang, T. C. Hou, Z. L. Wang, *Adv. Mater.* **2013**, *25*, 6094.
- [34] Y. F. Hu, J. Yang, Q. S. Jing, S. M. Niu, W. Z. Wu, Z. L. Wang, *ACS Nano* **2013**, *7*, 10424.
- [35] S. H. Wang, S. M. Niu, J. Yang, L. Lin, Z. L. Wang, *ACS Nano* **2014**, *8*, 12004.
- [36] D. Bhatia, W. Kim, S. Lee, S. W. Kim, D. Choi, *Nano Energy* **2017**, *33*, 515.
- [37] J. Yang, J. Chen, Y. Yang, H. L. Zhang, W. Q. Yang, P. Bai, Y. J. Su, Z. L. Wang, *Adv. Energy Mater.* **2014**, *4*, 9.
- [38] M. Y. Xu, P. H. Wang, Y. C. Wang, S. L. Zhang, A. C. Wang, C. L. Zhang, Z. J. Wang, X. X. Pan, Z. L. Wang, *Adv. Energy Mater.* **2018**, *8*, 9.
- [39] P. Cheng, H. Guo, Z. Wen, C. Zhang, X. Yin, X. Li, D. Liu, W. Song, X. Sun, J. Wang, Z. L. Wang, *Nano Energy* **2019**, *57*, 432.
- [40] S. M. Niu, Y. Liu, X. Y. Chen, S. H. Wang, Y. S. Zhou, L. Lin, Y. N. Xie, Z. L. Wang, *Nano Energy* **2015**, *12*, 760.
- [41] L. Lin, Y. Xie, S. Wang, W. Wu, S. Niu, X. Wen, Z. L. Wang, *ACS Nano* **2013**, *7*, 8266.
- [42] H. Zou, Y. Zhang, L. Guo, P. Wang, X. He, G. Dai, H. Zheng, C. Chen, A. C. Wang, C. Xu, Z. L. Wang, *Nat. Commun.* **2019**, *10*, 1427.